NIH Public Access
Author Manuscript
Traffic. Author manuscript; available in PMC 2012 August 1.

Published in final edited form as:
Traffic. 2011 August ; 12(8): 1000–1011. doi:10.1111/j.1600-0854.2011.01209.x.

Dynamics of native β-actin mRNA transport in the cytoplasm

Aaron W. Lifland[†], **Chiara Zurla**[†], **Joana Yu**[†], and **Philip J. Santangelo**[†,*]
[†] Wallace H. Coulter Department of Biomedical Engineering, Georgia Institute of Technology and Emory University, Atlanta, Georgia 30332

Abstract

Transport of mRNAs in the cytoplasm is essential for localization to translation sites and for post-transcriptional regulation. Utilizing single-RNA sensitive probes and real-time fluorescence microscopy, we accurately quantified the dynamics of native, non-engineered, β-actin mRNAs within the cytoplasm of epithelial cells and fibroblasts for the first time. Using single particle tracking and temporal analysis, we determined that native β-actin mRNAs, under physiologic conditions, exhibit bursts of intermittent, processive motion on microtubules, interspersed between time periods of diffusive motion, characterized by non-thermal enhanced diffusivity. When transport processes were perturbed via ATP-depletion, temperature reduction, dynamitin overexpression, and chemical inhibitors, processive motion was diminished or eliminated and diffusivity was reduced. These data support a model whereby processive, motor driven motion is responsible for long distance mRNA transport.

Keywords

RNA Imaging; Single Particle Tracking; Intracellular transport; RNA transport; Temporal Analysis; RNA regulation

INTRODUCTION

Messenger ribonucleic acids (mRNAs) are thought to serve as a key intermediary in gene expression through their specific and dynamic molecular composition (1). Transport of mRNAs in the cytoplasm is essential for localization to sites of translation and for the sorting to discrete cytoplasmic foci during post-transcriptional regulation (1–3). Owing to the high viscosity, significant crowding and inhomogeneous nature of the cytoplasm, active transport of mRNA is likely required even if the overall result is to evenly distribute individual mRNAs throughout the cell (4). Actin and microtubule-dependent motors, myosin, kinesin and dynein, have all been shown to be necessary for mRNA localization but their role in mRNA transport is not clear (5). Indeed, it may be obscured by non-enzymatic and indirect functional roles such as anchoring to the cytoskeleton or reshaping of the environment around the mRNA granules (6). In order to determine the contribution of molecular motors and the cytoskeleton to mRNA transport, it is essential to be able to visualize and track single mRNAs or single mRNA granules in live cells. Many cis and trans-acting factors responsible for the localization and regulation of mRNA have been identified; however, mechanistic information has been largely inferred from endpoint analysis, insertion of cis-acting sequences into transgenes, and delivery of synthetic transcripts into live cells (7–11). Since proper regulation of mRNAs requires the correct mRNA coding sequence, untranslated regions (UTRs), and the placement of exon junction

[*]Correspondence [philip.santangelo@bme.gatech.edu].

NIH-PA Author Manuscript
NIH-PA Author Manuscript
NIH-PA Author Manuscript

NIH-PA Author Manuscript

NIH-PA Author Manuscript

NIH-PA Author Manuscript

complexes (EJCs) during nuclear processing (12, 13), the study of unaltered, native transcripts is critical.

Among all the transcripts in the mammalian genome, β-actin mRNA represents a useful model system to investigate mRNA transport because its localization has been studied in different cell types such as fibroblasts, epithelial cells and neurons (14). Several mechanisms have been proposed for the transport of β-actin mRNA, including transport on microtubules, transport on microfilaments and diffusion throughout the cytoplasm (14–16). Initial reports using endpoint analysis and fluorescence in situ hybridization (FISH) in chicken and mouse embryonic fibroblasts, suggested that β-actin mRNA localization was dependent on actin filaments and that movement occurred along actin fibers (10, 17, 18). However, live cell experiments using the MS2-GFP system in COS7 cells showed that a reporter mRNA encoding the bacterial protein LacZ was actively transported along microtubules in the presence and absence of the zipcode binding protein (ZBP1) binding sequence, a key factor in β-actin mRNA localization. The presence of the ZBP1 binding site, however, increased the persistence of transport (8). While this microtubule dependent transport is consistent with live cell tracking studies of IMP1-containing granules (the human ZBP1 orthologue) (19), it is inconsistent with the FISH experiment results on native β-actin mRNA. Other reports using the MS2-GFP and MS2-YFP system with a reporter mRNA containing the β-actin coding sequence suggest that both transport and localization are diffusion dependent (13, 15, 16), controlled by the size of the mRNA and not by its sequence (16).

Here, we employed single-RNA sensitive multiply-labeled tetravalent imaging probes (MTRIPs) delivered into live cells to track the movement of native, non-engineered, β-actin mRNA at the single mRNA granule level and analyzed the data using standard deviation maps and single particle tracking with temporal analysis. This was done in order to establish the role of the different cytoskeletal elements in mRNA dynamics, in the attempt to provide clarity in the conflicting data in the field and test the hypotheses that the observed differences previously discussed might be cell type dependent, as recently proposed (14). For this purpose, experiments were performed in A549 cells, an epithelial cell line, as well as in primary human dermal fibroblasts (20). We demonstrated that native β-actin mRNAs, under physiologic conditions, exhibit bursts of intermittent, processive motion on microtubules, interspersed between time periods of diffusive motion, during which transport is aided by non-thermal forces, resulting in enhanced diffusivity. We demonstrate that the movement of the mRNA granules throughout the cytoplasm is mediated by processive, active transport, since it is ATP and temperature-dependent, and it relies on molecular motors. Moreover, we demonstrate that an intact microtubule network is required for mRNA transport in both epithelial cells and human fibroblasts.

RESULTS & DISCUSSION

MTRIPs targeting β-actin mRNA were previously shown to colocalize with ZBP1 and with Arp2 mRNAs in the protrusions of A549s and CEFs, and were shown to undergo directed motion in A549s (19). Preliminary live cell experiments using two MTRIPs targeting the β-actin mRNA coding region allowed the imaging and tracking of native granules in live cells for approximately one minute at 5 Hz frame rate during continuous imaging (20); however the nature of mRNA motion was not investigated nor was its cell type dependence addressed. Moreover, processes governing mRNA transport may occur on longer time scales than those previously utilized. Indeed, it's been proposed that mRNA may change between transport mechanisms within minutes (8).

In order to increase the observation time and avoid overlooking the contribution of different transport mechanisms due to temporal undersampling, we designed additional MTRIPs

NIH-PA Author Manuscript

NIH-PA Author Manuscript

NIH-PA Author Manuscript

targeting distinct sequences in both the coding region and 3′ UTR of native β-actin mRNAs (Table S1 in the Supporting Material). 3′ UTR probes were designed to avoid binding to the ZBP1, HuR, and TIA-1 binding sites (21–23). Probes were delivered into live cells via streptolysin-O (SLO) reversible permeabilization (20, 24–37). After recovery in complete growth medium, plasma membrane integrity was tested using an ethidium bromide exclusion assay. A small increase (2% to 6%) in ethidium bromide stained cells was observed in mock cells (no treatment) and in cells after SLO-mediated delivery of probes, while cells treated with triton X-100 showed 100% permeabilization (data not shown). This confirmed earlier results using ethidium homodimer and calcein AM assays, and propidium iodide exclusion that suggested near complete recovery of membrane integrity after the recovery phase (20, 27). To exclude the possibility that the additional probes were cross linking individual mRNAs into aggregates, we quantified the number of mRNA granules when 6 non-tetramerized ligands, and 2 or 6 MTRIP probes (probe sequences 1–6 in Table S1) were delivered into cells (Fig. 1 *A* and *B*). For the 2 MTRIP case, only probe sequences 1 and 2 (Table S1 in the Supporting Material) were used. Owing to the small diameter of the tetramerized probes (~5 nm) if crosslinking of mRNA were occurring, it would result in the reduction of the number of apparent granules, since the resulting mRNA would be smaller than the resolvable limit of the microscope (~250 nm). No significant difference ($p>0.5$ by Kruskal–Wallis analysis of variance) was observed in the number of mRNA granules in the three experimental conditions, indicating that aggregation of mRNAs does not occur (Fig. 1 *B*). Comparison between experiments performed with 6 linear probes, 2 MTRIPs and 6 MTRIPs showed that MTRIPs were consistently brighter than linear probes and the additional MTRIPs demonstrated an approximately two fold increase in the fluorescence intensity of detected native mRNA granules ($p<0.05$) (Fig. 1 *C*). This increase in intensity, along with the constant number of granules detected suggests that MTRIPs are specifically labeling β-actin mRNA granules and not non-specifically aggregating in the cell. The use of 6 MTRIPs allowed for an acquisition frame rate of 5 Hz and imaging time of over 5 minutes, considerably longer than imaging durations of previous single molecule sensitive mRNA tracking studies (8, 13, 38). A fast acquisition rate was chosen such that, frame-to-frame, mRNA granules moving at 1 μm/s would not move further than the resolution limit of the microscope (~250nm). Additionally, no change in the mRNA distribution was apparent when either linear or tetramerized probes were used (Fig. 1 *D–F*).

In order to exclude the possibility that the probes entered the cell by endocytosis or were sequestered in endosomes during the experiments, cells were fixed 15 min and 2 hrs post delivery and immunostained for early endosomal antigen 1 (EEA1), cluster of differentiation 63 (CD63) and lysosome associated membrane protein 1 (LAMP1), markers for early endosomes, late endosomes, and lysosomes respectively (Fig. S1 in the Supporting Material). These results were compared to those observed in a similar experimental setup using fluorescently labeled Neutravidin conjugated with the TAT peptide (NA-TAT), whose uptake was previously shown to depend on endocytosis (39). NA-TAT was shown to colocalize with all three endosomal markers after 2 hrs of incubation both by visual inspection and by Manders' overlap and Pearson's coefficients calculated on the reconstructed voxel (3D) data, confirming entry by an endocytic mechanism (Fig. S1 in the Supporting Material). These data are in good agreement with previous reports of low colocalization with endocytic proteins at early timepoints and a high degree of colocalization at later time points (39). In contrast, the low Manders' overlap and Pearson's coefficients exhibited by MTRIPs at the same time points demonstrated they do not colocalize with endosomal markers (Fig. S1 in the Supporting Material) confirming that SLO-mediated MTRIP entry does not proceed through the endocytic pathway nor are probes sequestered in endosomes while the experiments were performed. To statistically confirm that there is a significant difference between MTRIP delivery and endosomal uptake, an ANOVA on ranks was performed, pairing Pearson's and Manders' coefficients at the 2 hr

NIH-PA Author Manuscript

NIH-PA Author Manuscript

NIH-PA Author Manuscript

time point for MTRIP delivery and NA-TAT incubation. All pairs were confirmed to be statistically significant ($p<0.05$).

To demonstrate that the use of MTRIPs to target mRNAs does not bias our data to a subset of transcripts, β-actin mRNAs were simultaneously detected using MTRIPs delivered into live cells and, subsequently after fixation, using FISH as described in the material and methods section. Figure 2 shows the distribution of MTRIP probes and FISH staining in a representative A549 cell as well as their colocalization. Both probes prevailed throughout the cytoplasm in the perinuclear region and cell edge. Image intensity plots (Fig. 2D and H) demonstrated that MTRIP and FISH signals are coincident at the single granule level.

Finally, to demonstrate the molecular specificity of MTRIPs in targeting native β-actin mRNA, siRNA against β-actin was used to specifically lower the transcript copy number. β-actin mRNA levels were assessed 48 hr post delivery, using either qRT-PCR or fluorescence imaging (Fig. S2 in the Supporting Material). Both PCR and granule counting displayed a significant drop in β-actin mRNA upon siRNA delivery (90% and 80% respectively, $p>0.05$) when compared with control siRNA treated cells. Several factors may play a role in the discordance in the number of granules counted using MTRIPs compared with mRNA levels determined by RT-PCR including the presence of multiple mRNAs within individual granules, limitations in resolving and identifying diffraction limited objects, background from unbound probes and heterogeneity of the mRNA granules. Even with these complications in counting mRNA granules, the extent of observed knockdown clearly demonstrates the specificity of MTRIPs targeting of β-actin mRNA.

Live cell imaging was performed using MTRIPs with probe sequences 1–6 (Fig. 3 *A* and Movie S1 and Table S1 in the Supporting Material) and data were analyzed either by computing standard deviation (SD) maps for each image time series over short (seconds) or long (tens of seconds) time scales, or using single particle tracking. SD maps are pixel by pixel calculations of the standard deviation of the intensity calculated over given time lags that yield two dimensional representations of time series imaging data. High fluctuations in intensity over the time series correspond to high intensity values in the SD map and indicate particle movement through the area over the time scale analyzed (40, 41). SD maps, therefore, allow discrimination between fast movements of mRNA granules within the cells when analysis takes place over short time scales and slow or cumulative movements when analysis is performed over longer time scales. SD maps were used in place of maximal intensity projections because SD maps reduce signal from static particles and are less sensitive to loss of signal intensity by photobleaching. In A549 cells, short time scale analysis of cytoplasmic mRNAs revealed fast curvilinear movements, indicative of molecular motor-driven active transport (Fig. 3 *B*) and diffusive motion (Fig. 3 *C*). Active transport was observed to be intermittent and granules would often undergo several rounds of transport during the five minute imaging period. Some mRNA granules exhibited a coordinate motion as they would simultaneously begin moving collinearly and simultaneously stop (Fig. 3D and Movie S2 in the Supporting Material). SD maps revealed that these intermittent directed movements over time allowed the mRNAs to explore the entire cytoplasmic volume in ~300 seconds (Fig. 3E). mRNAs not undergoing such movements were observed to be either stalled or exhibited a random walk-like motion (Fig. 3C) and were observed in the perinuclear region as well as along the cell edges. Stalled granules displayed few, short (~5 s) time-scale movements (Fig. 3F), but motion was indeed observed over long (~100 s) time scales, particularly at the leading edge of cells (Fig. 3G and H). This motion suggested that these stalled granules were anchored to the cytoskeleton and moving according to extensions or retractions of the leading edge. In contrast, static mRNA granules in the perinuclear region did not exhibit either short or long time scale movements (Fig. 3I and J respectively).

NIH-PA Author Manuscript

NIH-PA Author Manuscript

NIH-PA Author Manuscript

Single particle tracking (SPT) allowed for a more detailed analysis of the dynamics of individual mRNAs (Fig. 4A–G). Figure 4A and Movie S3 in the Supporting Material show a typical particle trace of a β-actin mRNA granule within the cytoplasm of A549 cells with the corresponding SD map. Each particle trace was segmented using a temporal rolling window algorithm (42) in order to discriminate between states of active, processive motion, and passive, diffusive motion. This was done by calculating the square of the radius of gyration (R_G^2) for each mRNA granule along the rolling window; then Monte Carlo simulations were used to set a threshold such that there was less than a 1% chance that passive motion would be categorized as active transport or active transport categorized as passive (Fig. S3 in the Supporting Material) (43). Trajectory segments where R_G^2 exceeded the threshold of 0.05 μm^2 corresponded to linear increases in displacement, sustained increases in instantaneous velocity, and linear motion in the particle trace (Fig. 4B–D). We analyzed 60 independent particle tracks and obtained a cumulative histogram of the instantaneous velocities during active transport. A Gaussian fit of the histogram revealed a peak at 0.9 μm/s ±0.3μm/s (±s.d.) (Fig. 4E), which is in agreement with previous reports of mRNA transport in epithelial cells (8). The mean instantaneous velocity during the entire imaging time period was found to be lower (0.15 μm/s), as would be expected from averaging directed motion and diffusive states. This average velocity over entire particle paths is in good agreement with previous reports of the tracking of IMP1-containing granules (19). Interestingly, the histogram of the duration of time during which mRNAs displayed directed motion could not be well modeled by a single exponential decay, but rather by a log-normal fit with a median of 1.2s (Fig. 4G), indicating that active transport of the mRNAs may not follow simple first order kinetics. Segments categorized as passive transport were analyzed by calculating the mean square displacement (MSD) over a moving window and yielded a median apparent diffusion coefficient of 5.3×10^{-3} $\mu m^2/s$ (Fig. 4 *F*) based on a model of normal diffusion (44).

The observed fast, directed motion could either be due to molecular motors that are involved in mRNA transport or to inhomogeneities in the cytoplasm that cause apparent deviations from the stereotypical random walk. In order to demonstrate that the observed fast processive motion is a result of an enzymatically driven process rather than diffusion, mRNAs were tracked at 25°C or after depletion of ATP. The analysis of β-actin mRNAs in live cells incubated at 25°C showed a dramatic decrease in the number of granules undergoing directed motion (Fig. 5) while ATP depletion completely abolished directed motion (Fig. 5). To quantify the reduction in the number of processive motion events seen with temperature reduction, SD maps of independent 5 s intervals were generated and the fraction of mRNA undergoing processive motion during those intervals were counted. Incubation of the cells at 25°C resulted in an 80% decrease in the fraction of mRNA in processive motion (Fig. 6). The dramatic effect of ATP depletion was confirmed by the SD maps that revealed very little movement both over 5 s and 30 s time scales (Fig. 5). Single particle tracking analysis yielded an estimation of apparent diffusion constants of 1.1×10^{-3} $\mu m^2/s$ and 5.8×10^{-5} $\mu m^2/s$ for cells incubated at 25°C and ATP-depleted respectively (Fig. S4 in the Supporting Material). Both of these treatments were reversible, since removing the metabolic inhibitors or raising the temperature restored directed motion within an hour (Fig. 5 & 6 and data not shown). The observation that directed motion is dramatically decreased in these experimental conditions, as well as the apparent diffusion coefficients, implies that diffusion is not an efficient transport process for mRNAs, probably as a consequence of molecular crowding in the cytoplasm (4). Indeed, biophysical measurements of the relative diffusivity of synthetic polymers and DNA in the cytoplasm indicate that large structures such as mRNA transport granules will have limited diffusion in this cellular compartment (4, 45, 46). Moreover, molecular interactions of constituents of the mRNA granule, such as molecular motors, eEF1 or ZBP1, with the cytoskeleton, may be hindering the ability of the mRNA granules to diffuse freely (14). Our data indicate that enzymatically driven, ATP-

NIH-PA Author Manuscript

NIH-PA Author Manuscript

NIH-PA Author Manuscript

dependent transport is responsible for the capability of native mRNAs to explore the cytoplasm.

Transport of mRNA in the cytoplasm has previously been shown to depend on either microtubules or actin microfilaments, depending on the specific mRNA and model organism (5). For example, transport of mRNA on actin filaments has been observed for ASH1 mRNA in yeast, while transport in mammalian cells and drosophila embryos has been observed to be driven primarily by kinesin or dynein (5). The localization of β-actin mRNA has been shown to be dependent on actin cytoskeletal filaments in fibroblasts (10, 17) and, while it is hypothesized that transport of β-actin mRNA may occur along actin microfilaments (17), this has not been shown in a live cell. In order to determine the cytoskeletal element required for the transport of β-actin mRNA in A549 epithelial cells we used cytoskeleton disrupting agents to selectively depolymerize the microtubule or actin networks and observe the effects on the observed mRNAs fast directed motion. Disruption of microtubules using nocodazole, confirmed by immunofluorescence (Fig. S5 in the Supporting Material), hindered all mRNA directed motion (Fig. 5). Interestingly, β-actin mRNA granules appeared to aggregate after disruption of microtubules (Fig. S5 F). After verifying that nocodazole does not alter the centrosomes localization within cells (Figures S5 H and I) we demonstrated that the overall distribution of β-actin mRNA granules relative to the centrosome, was unchanged (Fig. S5 *G–I* in the Supporting Material). Particle tracking yielded an apparent diffusion coefficient of 2.5×10^{-4} $\mu m^2/s$ (Fig. S4 in the Supporting Material). This effect was reversible since removal of nocodazole from the media restored directed movement of mRNA granules (Fig. 5 and 6). In contrast, treatment with Cytochalasin D did not affect directed motion of mRNA granules despite the dramatic alteration of cell morphology (Fig. S6 in the Supporting Material and Fig. 6). Our data indicate that native mRNAs directed motion is dependent on an intact microtubule network and requires ATP. To further verify this, we incubated cells with blebbistatin, which selectively inhibits Myosin II activity (47), and, as expected, no alteration in mRNAs directed motion was observed (Fig. S6 in the Supporting Material and Fig. 6). However, when cells were treated with tetracaine, a promiscuous inhibitor of molecular motors (48, 49), directed motion was halted within 1 minute, and particle tracking of mRNA granules yielded a diffusion coefficient of 2.5×10^{-5} $\mu m^2/s$ (Figs. S4 and S6 in the Supporting Material and Fig. 6). To quantify the relative contributions of the microtubule dependent motors, kinesins and dynein, to the processive motion displayed by β-actin mRNA granules, cells were treated with EHNA, a chemical inhibitor of dynein or were transfected with p50/Dynamitin-GFP, which specifically causes the dissociation of the dynactin complex. The fraction of mRNA particles in processive motion was reduced by 60% after treatment with EHNA (Fig. S6 in the Supporting Material and Fig. 6) and after overexpression of p50 (Fig. S7). This suggests that both kinesin and dynein may play a significant role in β-actin mRNA transport. Further work will be necessary to determine the relative contribution of individual members of the kinesin family to mRNA motion.

To address whether microtubule dependent motion was specific to epithelial cells or if it was a more general mechanism of transport, the movement of β-actin mRNA in primary human dermal fibroblasts (HDFs) was analyzed before and after nocodazole treatment. As in the A549 cells, β-actin mRNA in fibroblasts exhibited motion indicative of molecular motor driven transport. However, in HDFs, the fraction of mRNA granules undergoing processive motion was notably lower than in A549s. To quantify this, the number of mRNA granules undergoing processive motion during independent 5s intervals were counted using SD maps for both A549s and HDFs. In A549s the fraction of mRNA granules undergoing processive motion during a 5s time span was 0.08, for HDFs this was reduced to 0.01 (Fig. S8 in the Supporting Material) ($p<0.05$). As in the A549 cells, processive motion was practically eliminated when the fibroblasts were treated with nocodazole, resulting in no apparent motor

NIH-PA Author Manuscript

NIH-PA Author Manuscript

NIH-PA Author Manuscript

driven motion (Fig. S8 in the Supporting Material). Particle tracking of mRNA granules in the nocodazole treated cells yielded an apparent diffusion coefficient of 4×10^{-4} $\mu m^2/s$ similar to the one obtained in A549s. These data suggest that molecular motor transport of β-actin mRNA is driven by microtubule dependent motors in both epithelial cells and fibroblasts and that in neither cell type is there long distance (>10 microns) transport of β-actin mRNA without an intact microtubule network. It is important to note that while the fraction of mRNA undergoing directed transport during any given 5s period is low, this transport is intermittent and granules switch between diffusive motion and directed transport. Our data indicate that nearly all mRNA granules will undergo at least one round of directed transport within 60s in A549s and 8 min in HDFs. Furthermore these data clearly indicate that the duration of the experimental time for live cell imaging is crucial when studying these processes. For example, live cell imaging, in an HDF, for 1s would require tracking 500 granules to capture directed motion of 1 mRNA granule. Short imaging times would also adversely affect particle trace segmentation by temporal analysis.

To better demonstrate the effect that intermittent processive motion has on RNA transport, Monte Carlo simulations were used to model diffusion and diffusion with intermittent processive motion. Simulations were performed using a diffusion coefficient of 0.005 $\mu m^2/s$ and a velocity of 1 μm/s calculated from SPT analysis and over time periods of 5 min and 30 min for comparison with data presented here, and to demonstrate the effect of intermittent processive motion over longer time scales. Probabilities for switching into an active state were fixed at 0.016 s^{-1}, while probabilities of leaving an active state were dependent upon how long particles were in the state, and were calculated from active state durations from SPT experiments. When RNA transport was simulated over 5 min, median displacement was increased from 1.1 um to 3.8 um (Fig. 7 dashed lines) when intermittent processive motion was added to normal diffusion. More strikingly, when transport was simulated over a 30 min period, median displacement increased from 2.6 um to 23 um with the addition of intermittent processive motion (Fig. 7 solid lines).

CONCLUSION

We have described here the microtubule-dependent transport of native β-actin mRNAs in the cytoplasm of epithelial cells and fibroblasts. In both cell lines, transport was shown to be processive and occurred intermittently over 5 minutes. Without an intact microtubule network, mRNA motion was dramatically impaired, indicating that diffusion is unlikely a biologically relevant mechanism for mRNA granule transport in the cytoplasm. While this is predicted from previously published biophysical measurements of macromolecules of similar size and molecular weight as mRNA, controversy still exists on the importance of diffusion in mRNA localization (13, 15, 16).

Interestingly, the experiments performed with nocodazole, with ATP-depletion compounds and tetracaine in A549 cells, not only eliminated processive motion of β-actin mRNA, but also yielded consistently lower apparent diffusion coefficients than those performed in control conditions. This suggests that non-processive mRNA transport may be the result of a superposition of diffusion, cytoskeletal remodeling, and indirect action of molecular motors on the adjacent cytoplasm. These factors have been proposed to have a significant effect on large particles (such as vesicles) attached to the cytoskeleton (50) but have not, as of yet, been reported to effect the transport of mRNA.

The use of MTRIPs in imaging native mRNA in live cells has many advantages, such as the probes are bright and can achieve single-molecule sensitivity, they are sufficiently photostable for single particle tracking over relevant time scales, and they can be used simultaneously with fluorescent proteins in live cells. MTRIPs are not only specific, but they

NIH-PA Author Manuscript

NIH-PA Author Manuscript

NIH-PA Author Manuscript

do not significantly increase the molecular weight or size of an mRNA granule. However, certain considerations must be taken into account when using MTRIPs. MTRIPs bind to native mRNA sequences and, therefore, care must be taken in the selection of their sequences to avoid blocking of RNA binding protein sites. Careful thresholding of fluorescence intensity against unbound probes is also necessary to exclude background from analysis, as MTRIPs are not fluorogenic but are particularly bright. Finally, there is still little information on the effect of MTRIPs on RNA stability and decay. For long half-life mRNA, such as β-actin, such effects are minimized, but it may be an important consideration in studies on shorter lived mRNAs.

MATERIALS & METHODS

MTRIPS

MTRIPS were prepared as previously described (20). Briefly, 2 -O-methyl RNA-DNA oligonucleotide chimeras were designed with a 5 -biotin and dT-C6-NH2 internal modifications (Biosearch Technologies, Novato, CA). MTRIPs were assembled by first conjugating either Cy3B-NHS ester fluorophores (GE Heathcare, Buckinghamshire, England) or Dylight 649-NHS ester fluorophores (Pierce, Rockford, IL) to the oligonucleotide amine groups using the manufacturer's protocol. Labeled oligonucleotides were then tetramerized by incubation with Neutravidin (Pierce). MTRIPs targeting different mRNA sequences (Table S1 in the Supporting Material) were assembled separately prior to delivery.

Cells and Cell Culture

A549 lung carcinoma cells (ATCC, Manassas, VA) and primary human dermal fibroblasts (Lonza, Basel, Switzerland) were maintained in High Glucose DMEM (Lonza, Basel, Switzerland) with 10% fetal bovine serum (Hyclone, Logan, UT), 100 U ml^{-1} penicillin, and 100 μg ml^{-1} streptomycin (Invitrogen, Carlsbad, CA). Cells were plated one day prior to imaging.

Probe Delivery

For probe delivery, cells were washed in DPBS (Lonza) -Ca^{2+} -Mg^{2+}, and then incubated 0.2U ml^{-1} activated streptolysin-O (SLO) (Sigma) in OptiMEM (Invitrogen) containing 15nM of each MTRIP for 10 min at 37°C. Delivery media was replaced with growth media for 15 min to restore membrane integrity before live cell imaging or fixation.

Delivery of Neutravidin-TAT

Neutravidin was fluorescently labeled with Cy3B according to the manufacturer's protocol. Labeled Neutravidin was subsequently conjugated to biotin-TAT peptide (Anaspec, Fremont, CA) by incubation at room temperature at a 1:40 molar ratio. Unbound biotin-TAT peptides were separated from the conjugate using a 30K MWCO centrifugal filter. A549 cells were incubated with 250 nM NA-TAT conjugates in normal growth media for 15 min or 2 hrs, fixed and immunostained as described.

Immunofluorescence

Cells were fixed for 10 min in 4% paraformaldehyde (Electron Microscopy Sciences, Hatfield, PA) and they were then immunostained for Early Endosomal Antigen 1 (mouse anti-EEA1, BD Biosciences, San Jose, CA), Cluster of Differentiation 63 (mouse anti-CD63, Developmental Studies Hybridoma Bank, Iowa City, IA), Lysosomal-associated membrane protein 1 (mouse anti-LAMP1, Developmental Studies Hybridoma Bank), β-tubulin (Invitrogen), or γ-tubulin (Sigma) as described (51) or by manufacturers' protocol.

NIH-PA Author Manuscript

NIH-PA Author Manuscript

NIH-PA Author Manuscript

Alexa fluor 488 Phalloidin was used to stain actin fibers. Cells were subsequently stained with DAPI (Invitrogen) and mounted on slides using Prolong gold (Invitrogen).

Drugs

After probe delivery, cells were incubated for 1 hr in glucose free DMEM (Invitrogen) containing 60 mM 2-deoxy-d-glucose (2DG) (CalBioChem, San Diego, CA) and 10 mM sodium azide (NaN_3) (VWR, West Chester, PA) for ATP depletion, for 90 min with 1 μM cytochalasin D (Sigma) for actin depolymerization, for 90 min with 4 μM nocodazole (Sigma) for microtubule depolymerization, and for 15 min with 1 mM erythro-9-(2-Hydroxy-3-nonyl)-adenine hydrochloride (EHNA) (Sigma). After incubation, live cell imaging was performed in Leibovitz L15 media supplemented with the appropriate drug. Drug recovery was achieved by replacing the drug-containing media with growth media. Tetracaine (Sigma) and blebbistatin (Sigma) were used at 100 μM and 50 μM in Leibovitz L15 media respectively and cells were imaged immediately.

p50/Dynamitin-GFP expression

A plasmid expressing p50/Dynamitin-GFP (supplied by Dr. Richard Vallee) was transfected into A549 cells using the Neon Transfection System (Invitrogen) following the manufacturers' protocol for 10μl electroporation volumes. Assays were carried out 24 hrs post-transfection in cells exhibiting GFP florescence indicative of efficient transfection and exhibiting normal cellular morphology.

siRNA delivery and qRT-PCR

A549 cells were transfected with 200 nM control siRNA or siRNA targeting β-actin mRNA (On target plus non targeting siRNA #1 and smart pool respectively, Dharmacon thermo Scientific) via electroporation using the Neon system (Invitrogen) according to manufacturer instructions. Transfections were performed in duplicates and a set of control cells were also plated. 48h post transfection MTRIPs targeting β-actin mRNA were delivered to a set of cells, which were subsequently fixed, stained with phalloidin and DAPI and mounted. The second set of cells was used for total RNA extraction using the RNeasy Mini kit (Qiagen). Total RNA was subsequently checked for integrity via agarose gel electrophoresis and quantified via UV-VIS spectrometry. 1μg total RNA was used for cDNA synthesis using the RT^2 first strand kit (SA biosciences) according to the manufacturer instructions. 1μl of the product was then used for qRT-PCR using the Real-time RT^2 qPCR primer assay (SYBR green) in the presence of human ACTB and GAPDH gene-specific primers (SA bioscences). qRT-PCR was performed using a ABI StepOnePlus real-time PCR system (Applied biosciences).

Fluorescence in situ hybridization (FISH)

MTRIPs labeled with Dylight 649 targeting β-actin mRNA (probe sequences 2 and 7 in Table S1) were delivered into A549s as described above. Cells were subsequently fixed in 4% paraformaldehyde, permeabilized in 70% ethanol overnight, rinsed in PBS three times and incubated for 2hr at 55°C in hybridization buffer (2×SSC (Ambion), 100 μg BSA, 10% dextran sulfate, 50 μg tRNA, 70 % formamide, 50 μg salmon sperm DNA and probes at 1 nM each). Probes used for FISH were linear Cy3B-labeled nucleic acid ligands (probe sequences 1, and 3–6 in Table S1). After hybridization, cells were rinsed with 2×SSC for 5 min, 10% fomamide in 2×SSC for 10 min and in 2×SSC for 5 min. Nuclei were stained using DAPI (Invitrogen) and cells were mounted on slides using Prolong gold (Invitrogen).

NIH-PA Author Manuscript

NIH-PA Author Manuscript

NIH-PA Author Manuscript

Fixed and Live Cell Microscopy

For live cell imaging, cells were plated in Bioptechs T4 plates (Bioptechs, Butler, PA) and growth media was replaced with Leibovitz L15 CO_2 independent media (Invitrogen) supplemented with 10% FBS for live cell imaging. Bioptechs dishes were maintained at 37°C using a Bioptechs Delta T system and an objective heater. For fixed cell imaging, cells were grown on No. 1.5 coverslips and fixed and immunostained after delivery of MTRIPS. Images were taken on an Axiovert 200M microscope (Zeiss, Oberkochen, Germany) with a 63x NA 1.4 Plan Apochromat primary objective and an ORCA-ER AG camera (Hamamatsu, Hamamatsu City, Japan). For ethidium bromide exclusion assays, a 20x NA 0.4 Plan Neofluar was used. Fluorescent filter sets used were 49004 ET-Cy3 for live cell imaging and 89000 Sedat Quad - ET for multiple wavelength imaging (Chroma, Bellows Falls, VT). All imaging experiments were performed using the Volocity acquisition software (Improvision, Waltham, MA). Image stacks were recorded at 200nm intervals for fixed cell samples to adequately sample volumes for iterative deconvolution.

Confocal Imaging

Images were captured on a Zeiss LSM 510 Meta using a 63x, NA 1.4 Plan-Apochromat objective. Resolution was set to 1024x1024. Files were imported into Volocity and linearly contrast enhanced for display.

Image Processing and analysis

All live and fixed cell images were deconvolved using Volocity's deconvolution algorithms. Image Z-stacks were deconvolved using iterative restoration and live cell movies were deconvolved using fast restoration. Granule counting and intensity quantification as well as Manders' and Pearson's coefficients were computed in Volocity and imported into Excel (Microsoft, Redmond, WA) or Sigma Plot (Systat, Chicago, IL for plotting. Kruskal–Wallis and ANOVA statistical tests were performed in MATLAB (The MathWorks, Natick, MA) or Sigma Plot. Images presented have been linearly contrast enhanced for clarity. All calculations were performed directly on unenhanced, deconvolved data. Standard deviation maps were computed using the ZProject plugin for NIH ImageJ on deconvolved image sets exported in Tiff format. Intensity profile plots were generated in ImageJ using the RGB profiler plugin.

Two dimensional random walk simulations with and without directed motion were performed in MATLAB using a fixed step size and a random angle. For threshold determination in SPT experiments a diffusion constant of 1×10^{-2} $\mu m^2/s$ and a velocity of 1 μm/s for directed motion was selected to ensure accurate discrimination between diffusive states and processive motion.

Mean square displacements were calculated by averaging independent particle tracks and by averaging independent time windows within tracks. Linear fitting was performed in Excel.

Single particle tracking

Single particle tracking was performed in Volocity. For experiments performed at 25°C or in the presence of tetracaine, nocodazole, or ATP depletion drugs, mRNA granules were tracked automatically using Volocity's tracking algorithms. For all other experimental conditions, tracking was performed manually using Volocity's manual tracking. Rolling window temporal analysis was performed in MATLAB with custom routines. Histograms were generated in Sigma Plot. Preliminary analysis was performed using a two parameter joint probability distribution (radius of gyration and eigen value ratio) to discriminate diffusive states and processive motion. However, the eigen value ratio was found to be unnecessary and for simplification only the radius of gyration was subsequently used.

NIH-PA Author Manuscript

NIH-PA Author Manuscript

NIH-PA Author Manuscript

Ethidium Bromide Exclusion Assay

A549 cells were grown to confluence on glass bottom petri dishes. Cells were mock treated with OptiMEM, SLO permeabilized and recovered as described above, or treated with 0.2% Triton X-100 in PBS. Cells were then incubated with Hoechst 33342 (Invitrogen) at 0.1μg/ml in DMEM for 30 min and subsequently incubated with 12 μM ethidium bromide (EMD) for 15 min. Media was then replaced with OptiMEM and cells were immediately imaged.

Supplementary Material

Refer to Web version on PubMed Central for supplementary material.

Acknowledgments

The authors thank Dr. Michael Saxton for his informative correspondence, Dr. Richard Vallee for supplying the p50/Dynamitin-GFP plasmid, and Dr. Brani Vidakovic for assistance with the statistical tests performed. We would like to also acknowledge the Institute of Bioengineering and Biosciences at Georgia Tech for use of the ABI real-time PCR instrument and the LSM 510 confocal microscope.

GRANTS

Support was provided by the Georgia Tech Administration and by the NIH (EB009455 and GM094198).

References

1. Anderson P, Kedersha N. RNA granules: post-transcriptional and epigenetic modulators of gene expression. Nat Rev Mol Cell Biol. 2009; 10(6):430–436. [PubMed: 19461665]
2. Holt CE, Bullock SL. Subcellular mRNA localization in animal cells and why it matters. Science. 2009; 326(5957):1212–1216. [PubMed: 19965463]
3. Martin KC, Ephrussi A. mRNA localization: gene expression in the spatial dimension. Cell. 2009; 136(4):719–730. [PubMed: 19239891]
4. Luby-Phelps K. Cytoarchitecture and physical properties of cytoplasm: volume, viscosity, diffusion, intracellular surface area. Int Rev Cytol. 2000; 192:189–221. [PubMed: 10553280]
5. Jansen RP. mRNA localization: message on the move. Nat Rev Mol Cell Biol. 2001; 2(4):247–256. [PubMed: 11283722]
6. Delanoue R, Davis I. Dynein anchors its mRNA cargo after apical transport in the Drosophila blastoderm embryo. Cell. 2005; 122(1):97–106. [PubMed: 16009136]
7. Bertrand E, Chartrand P, Schaefer M, Shenoy SM, Singer RH, Long RM. Localization of ASH1 mRNA particles in living yeast. Mol Cell. 1998; 2(4):437–445. [PubMed: 9809065]
8. Fusco D, Accornero N, Lavoie B, Shenoy SM, Blanchard JM, Singer RH, Bertrand E. Single mRNA molecules demonstrate probabilistic movement in living mammalian cells. Curr Biol. 2003; 13(2):161–167. [PubMed: 12546792]
9. Zimyanin VL, Belaya K, Pecreaux J, Gilchrist MJ, Clark A, Davis I, St Johnston D. In vivo imaging of oskar mRNA transport reveals the mechanism of posterior localization. Cell. 2008; 134(5):843–853. [PubMed: 18775316]
10. Sundell CL, Singer RH. Requirement of microfilaments in sorting of actin mRNAs. Science. 1991; 253:1275–1277. [PubMed: 1891715]
11. Wilkie GS, Davis I. Drosophila wingless and pair-rule transcripts localize apically by dynein-mediated transport of RNA particles. Cell. 2001; 105(2):209–219. [PubMed: 11336671]
12. Hachet O, Ephrussi A. Splicing of oskar RNA in the nucleus is coupled to its cytoplasmic localization. Nature. 2004; 428(6986):959–963. [PubMed: 15118729]
13. Ben-Ari Y, Brody Y, Kinor N, Mor A, Tsukamoto T, Spector DL, Singer RH, Shav-Tal Y. The life of an mRNA in space and time. J Cell Sci. 2010; 123(Pt 10):1761–1774. [PubMed: 20427315]
14. Condeelis J, Singer RH. How and why does beta-actin mRNA target? Biol Cell. 2005; 97(1):97–110. [PubMed: 15601261]

NIH-PA Author Manuscript

NIH-PA Author Manuscript

NIH-PA Author Manuscript

15. Yamagishi M, Ishihama Y, Shirasaki Y, Kurama H, Funatsu T. Single-molecule imaging of beta-actin mRNAs in the cytoplasm of a living cell. Exp Cell Res. 2009; 315(7):1142–1147. [PubMed: 19245805]

16. Yamagishi M, Shirasaki Y, Funatsu T. Size-dependent accumulation of mRNA at the leading edge of chicken embryo fibroblasts. Biochem Biophys Res Commun. 2009; 390(3):750–754. [PubMed: 19835844]

17. Latham VM, Yu EH, Tullio AN, Adelstein RS, Singer RH. A Rho-dependent signaling pathway operating through myosin localizes beta-actin mRNA in fibroblasts. Curr Biol. 2001; 11(13): 1010–1016. [PubMed: 11470405]

18. Johnsson AK, Karlsson R. Microtubule-dependent localization of profilin I mRNA to actin polymerization sites in serum-stimulated cells. Eur J Cell Biol. 2010; 89(5):394–401. [PubMed: 20129697]

19. Nielsen FC, Nielsen J, Kristensen MA, Koch G, Christiansen J. Cytoplasmic trafficking of IGF-II mRNA-binding protein by conserved KH domains. J Cell Sci. 2002; 115(Pt 10):2087–2097. [PubMed: 11973350]

20. Santangelo PJ, Lifland AW, Curt P, Sasaki Y, Bassell GJ, Lindquist ME, Crowe JE Jr. Single molecule-sensitive probes for imaging RNA in live cells. Nat Methods. 2009; 6(5):347–349. [PubMed: 19349979]

21. Lopez de Silanes I, Galban S, Martindale JL, Yang X, Mazan-Mamczarz K, Indig FE, Falco G, Zhan M, Gorospe M. Identification and functional outcome of mRNAs associated with RNA-binding protein TIA-1. Mol Cell Biol. 2005; 25(21):9520–9531. [PubMed: 16227602]

22. Lopez de Silanes I, Zhan M, Lal A, Yang X, Gorospe M. Identification of a target RNA motif for RNA-binding protein HuR. Proc Natl Acad Sci U S A. 2004; 101(9):2987–2992. [PubMed: 14981256]

23. Kislauskis EH, Zhu X, Singer RH. Sequences responsible for intracellular localization of beta-actin messenger RNA also affect cell phenotype. J Cell Biol. 1994; 127(2):441–451. [PubMed: 7929587]

24. Santangelo P, Nitin N, LaConte L, Woolums A, Bao G. Live-cell characterization and analysis of a clinical isolate of bovine respiratory syncytial virus, using molecular beacons. J Virol. 2006; 80(2): 682–688. [PubMed: 16378971]

25. Barry EL, Gesek FA, Friedman PA. Introduction of antisense oligonucleotides into cells by permeabilization with streptolysin O. Biotechniques. 1993; 15(6):1016–1018. 1020. [PubMed: 8292333]

26. Bhakdi S, Weller U, Walev I, Martin E, Jonas D, Palmer M. A guide to the use of pore-forming toxins for controlled permeabilization of cell membranes. Med Microbiol Immunol. 1993; 182(4): 167–175. [PubMed: 8232069]

27. Paillasson S, Van De Corput M, Dirks RW, Tanke HJ, Robert-Nicoud M, Ronot X. In situ hybridization in living cells: detection of RNA molecules. Exp Cell Res. 1997; 231(1):226–233. [PubMed: 9056430]

28. Giles RV, Spiller DG, Grzybowski J, Clark RE, Nicklin P, Tidd DM. Selecting optimal oligonucleotide composition for maximal antisense effect following streptolysin O-mediated delivery into human leukaemia cells. Nucleic Acids Res. 1998; 26(7):1567–1575. [PubMed: 9512525]

29. Spiller DG, Giles RV, Grzybowski J, Tidd DM, Clark RE. Improving the intracellular delivery and molecular efficacy of antisense oligonucleotides in chronic myeloid leukemia cells: a comparison of streptolysin-O permeabilization, electroporation, and lipophilic conjugation. Blood. 1998; 91(12):4738–4746. [PubMed: 9616172]

30. Clark RE, Grzybowski J, Broughton CM, Pender NT, Spiller DG, Brammer CG, Giles RV, Tidd DM. Clinical use of streptolysin-O to facilitate antisense oligodeoxyribonucleotide delivery for purging autografts in chronic myeloid leukaemia. Bone Marrow Transplant. 1999; 23(12):1303–1308. [PubMed: 10414920]

31. Walev I, Bhakdi SC, Hofmann F, Djonder N, Valeva A, Aktories K, Bhakdi S. Delivery of proteins into living cells by reversible membrane permeabilization with streptolysin-O. Proc Natl Acad Sci U S A. 2001; 98(6):3185–3190. [PubMed: 11248053]

NIH-PA Author Manuscript

NIH-PA Author Manuscript

NIH-PA Author Manuscript

32. Santangelo PJ, Nix B, Tsourkas A, Bao G. Dual FRET molecular beacons for mRNA detection in living cells. Nucleic Acids Res. 2004; 32(6):e57. [PubMed: 15084672]
33. Santangelo PJ, Nitin N, Bao G. Direct visualization of mRNA colocalization with mitochondria in living cells using molecular beacons. J Biomed Opt. 2005; 10(4):44025. [PubMed: 16178658]
34. Abe H, Kool ET. Flow cytometric detection of specific RNAs in native human cells with quenched autoligating FRET probes. Proc Natl Acad Sci U S A. 2006; 103(2):263–268. [PubMed: 16384914]
35. Santangelo PJ, Bao G. Dynamics of filamentous viral RNPs prior to egress. Nucleic Acids Res. 2007; 35(11):3602–3611. [PubMed: 17485480]
36. Rhee WJ, Santangelo PJ, Jo H, Bao G. Target accessibility and signal specificity in live-cell detection of BMP-4 mRNA using molecular beacons. Nucleic Acids Res. 2008
37. Utley TJ, Ducharme NA, Varthakavi V, Shepherd BE, Santangelo PJ, Lindquist ME, Goldenring JR, Crowe JE Jr. Respiratory syncytial virus uses a Vps4-independent budding mechanism controlled by Rab11-FIP2. Proc Natl Acad Sci U S A. 2008; 105(29):10209–10214. [PubMed: 18621683]
38. Vargas DY, Raj A, Marras SA, Kramer FR, Tyagi S. Mechanism of mRNA transport in the nucleus. Proc Natl Acad Sci U S A. 2005; 102(47):17008–17013. [PubMed: 16284251]
39. Rinne J, Albarran B, Jylhava J, Ihalainen TO, Kankaanpaa P, Hytonen VP, Stayton PS, Kulomaa MS, Vihinen-Ranta M. Internalization of novel non-viral vector TAT-streptavidin into human cells. BMC Biotechnol. 2007; 7:1. [PubMed: 17199888]
40. Cai D, Verhey KJ, Meyhofer E. Tracking single Kinesin molecules in the cytoplasm of mammalian cells. Biophys J. 2007; 92(12):4137–4144. [PubMed: 17400704]
41. Cai D, McEwen DP, Martens JR, Meyhofer E, Verhey KJ. Single molecule imaging reveals differences in microtubule track selection between Kinesin motors. PLoS Biol. 2009; 7(10):e1000216. [PubMed: 19823565]
42. Arcizet D, Meier B, Sackmann E, Radler JO, Heinrich D. Temporal analysis of active and passive transport in living cells. Phys Rev Lett. 2008; 101(24):248103. [PubMed: 19113674]
43. Saxton MJ. Single-particle tracking: models of directed transport. Biophys J. 1994; 67(5):2110–2119. [PubMed: 7858148]
44. Saxton MJ, Jacobson K. Single-particle tracking: applications to membrane dynamics. Annu Rev Biophys Biomol Struct. 1997; 26:373–399. [PubMed: 9241424]
45. Lukacs GL, Haggie P, Seksek O, Lechardeur D, Freedman N, Verkman AS. Size-dependent DNA mobility in cytoplasm and nucleus. J Biol Chem. 2000; 275(3):1625–1629. [PubMed: 10636854]
46. Seksek O, Biwersi J, Verkman AS. Translational diffusion of macromolecule-sized solutes in cytoplasm and nucleus. J Cell Biol. 1997; 138(1):131–142. [PubMed: 9214387]
47. Straight AF, Cheung A, Limouze J, Chen I, Westwood NJ, Sellers JR, Mitchison TJ. Dissecting temporal and spatial control of cytokinesis with a myosin II Inhibitor. Science. 2003; 299(5613):1743–1747. [PubMed: 12637748]
48. Miyamoto Y, Muto E, Mashimo T, Iwane AH, Yoshiya I, Yanagida T. Direct inhibition of microtubule-based kinesin motility by local anesthetics. Biophys J. 2000; 78(2):940–949. [PubMed: 10653806]
49. Tsuda Y, Mashimo T, Yoshiya I, Kaseda K, Harada Y, Yanagida T. Direct inhibition of the actomyosin motility by local anesthetics in vitro. Biophys J. 1996; 71(5):2733–2741. [PubMed: 8913610]
50. Brangwynne CP, Koenderink GH, MacKintosh FC, Weitz DA. Intracellular transport by active diffusion. Trends Cell Biol. 2009; 19(9):423–427. [PubMed: 19699642]
51. Lifland AW, Zurla C, Santangelo PJ. Single Molecule Sensitive Multivalent Polyethylene Glycol Probes for RNA Imaging. Bioconjug Chem. 2010

NIH-PA Author Manuscript

NIH-PA Author Manuscript

NIH-PA Author Manuscript

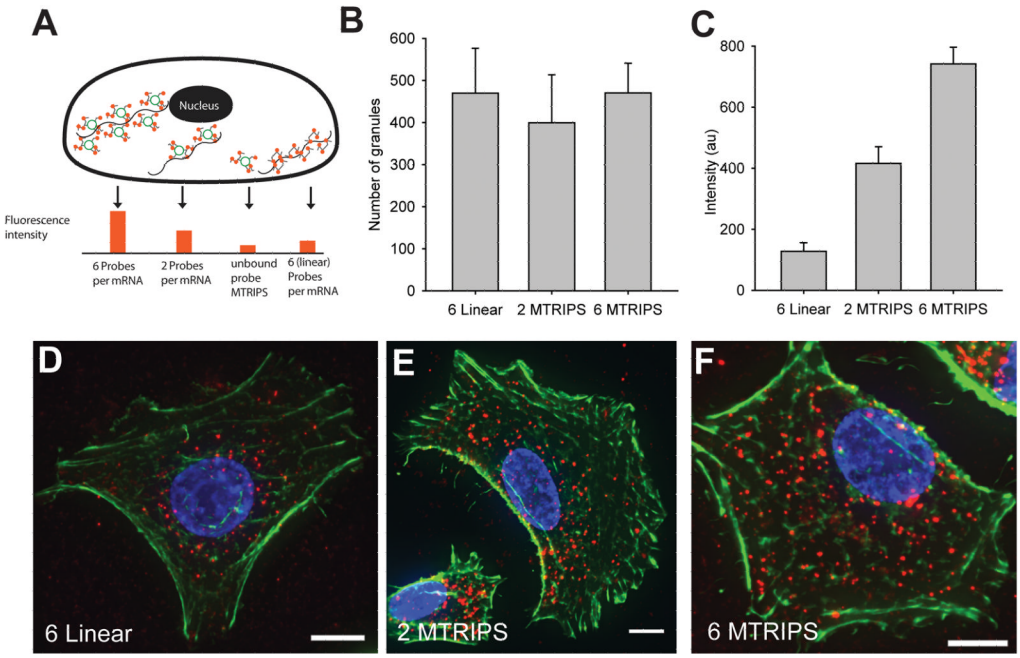

FIGURE 1.

mRNA targeting by MTRIPs. (*A*) Schematic representation of the detection method showing expected fluorescence intensity when 6 or 2 MTRIPs, or 6 linear probes target β-actin mRNA molecules and comparison with an unbound MTRIP probe. (*B*) Quantification of the average number of mRNA granules detected using 6 linear probes and 2 or 6 MTRIPs, demonstrating MTRIPs do not aggregate mRNAs. (C) Average fluorescence intensity when β-actin mRNA is targeted by 2 or 6 MTRIPs or 6 linear probes. Extended view of β-actin mRNAs targeted by 6 linear probes (D) 2 and 6 MTRIPs (E and F) (red) demonstrating the typical distribution of β-actin mRNA. Nuclei were stained with DAPI (blue) and the actin fibers were stained with phalloidin (green). Scale bars are 10 um.

NIH-PA Author Manuscript
NIH-PA Author Manuscript
NIH-PA Author Manuscript

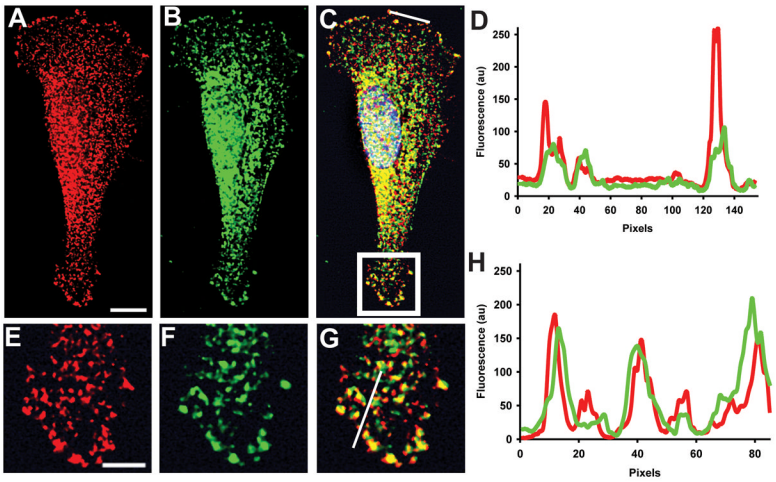

FIGURE 2.

MTRIPs colocalize with FISH probes targeting β-actin mRNA and exhibit a similar subcellular distribution. MTRIPs labeled with Dylight 649 (B green) were delivered into live A549 cells, which were subsequently fixed and stained for β-actin mRNA using Cy3B labeled linear FISH probes (A red). Colocalization of MTRIPs and FISH probes is demonstrated in the merged figure (C), where the magnification of a boxed region is shown in (E–G). Fluorescence intensity profiles in (D) and (H) show intensities along the white lines in C and G respectively, and demonstrate colocalization of probes at the single granule level. The nucleus is stained with DAPI (blue) and the image shown is a single deconvolved plane. Intensity profiles were generated from deconvolved images. Scale bars in (A) and (C) are 10 μm and 5 μm respectively.

NIH-PA Author Manuscript

NIH-PA Author Manuscript

NIH-PA Author Manuscript

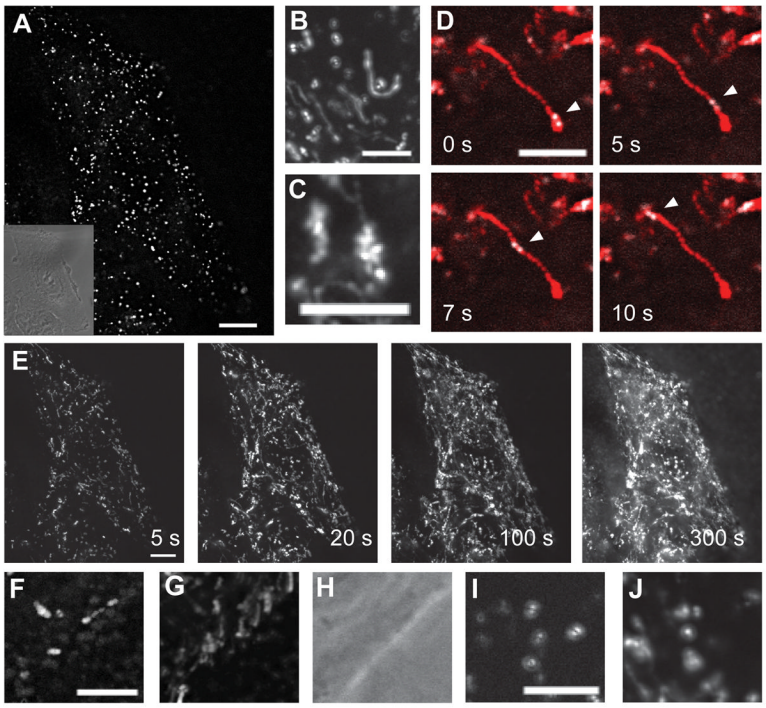

FIGURE 3.

Standard deviation (SD) maps of β-actin mRNA dynamics in live A549 cells. (*A*) A single optical plane at one time point showing well spaced distribution of β-actin mRNA granules. Inset shows the phase contrast image of the same cell. (*B*) SD map over 14 s of imaging showing mRNA granules undergoing processive motion. (*C*) SD map over 40 s of imaging showing mRNA granules undergoing diffusive motion. (*D*) Time series of two particles (white) undergoing coordinated movement overlaid to the corresponding SD map (red). (*E*) SD maps s of the same cell as in (*A*) calculated over 5 s, 20 s, 100 s, and 300. mRNA display an increase in the area explored as analysis is performed on larger time scales. SD map of mRNA granules near the leading edge of a cell calculated over (*F*) 5 s and (*G*) 120 s. mRNA are nearly static as the 5 s time scale but at longer time scales appear to undergo slow movement. (*H*) Phase contrast image showing edge of cell at the beginning of the time series for (*F*) and (*G*). SD map of particles near the nucleus of a cell calculated over (*I*) 5 s and (*J*) 120 s show almost no movement even over the longer time scales. Scale bars are 10 μm in (*A*,*E*,*D*) and are 5 μm in the remaining images.

NIH-PA Author Manuscript
NIH-PA Author Manuscript
NIH-PA Author Manuscript

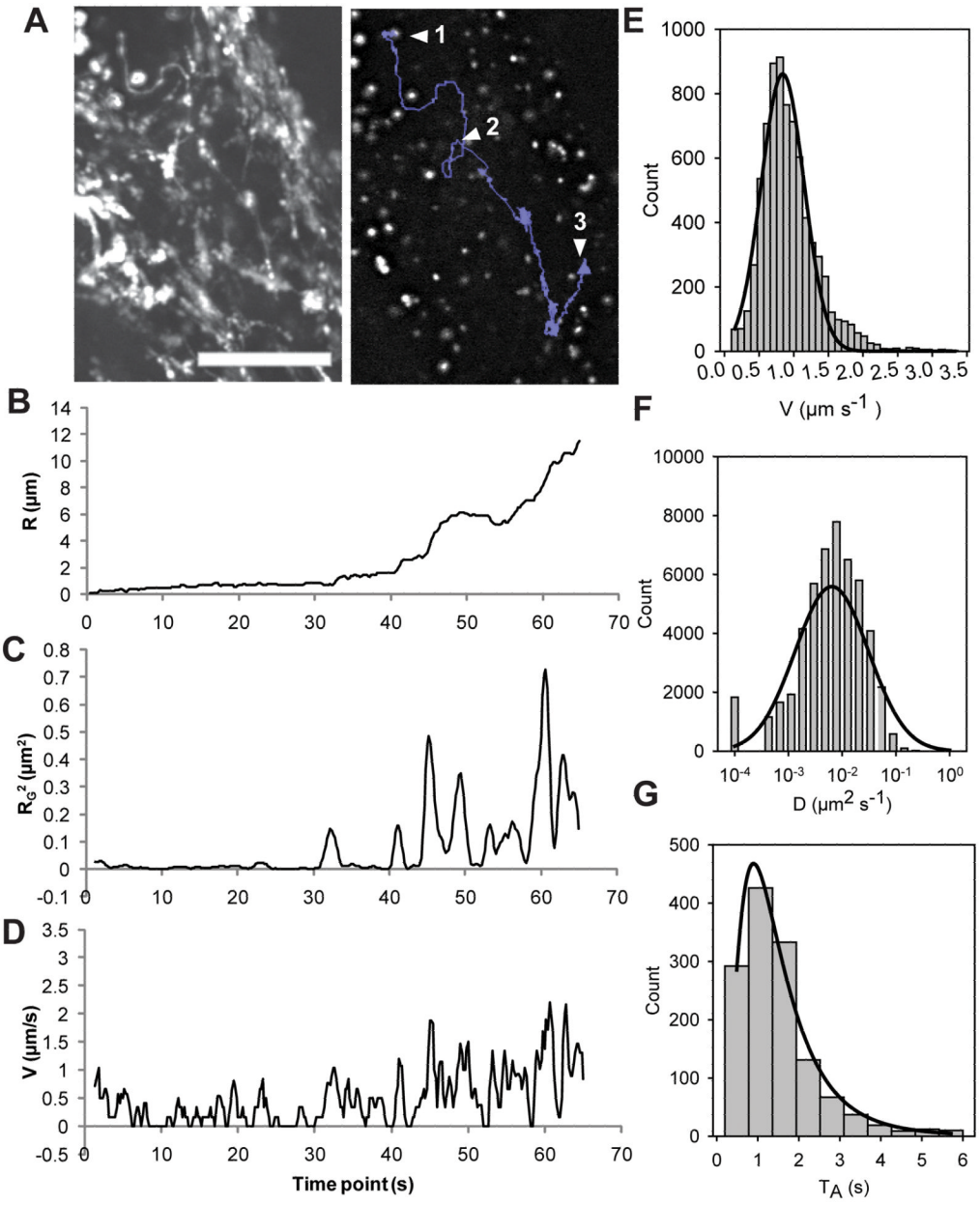

FIGURE 4.

Single particle tracking analysis of β-actin mRNA in an A549 cell.(*A*) SD map (right) over 120 s of imaging and particle track (Purple, left) showing a single mRNA granule initial position (1), position at 60 s (2) and final position (3); scale bar is 10 μm. (*B*) Overall displacement, (*C*) square of the radius of gyration determined from a rolling window of 1.6 s and (*D*) instantaneous velocity of the mRNA granule shown in (*A*) over 60 s of analysis. Cumulative histograms calculated from 60 independent particle tracks showing (*E*) instantaneous velocities during processive motion states (black line is a Gaussian fit), (*F*) diffusion coefficients during diffusive states calculated over rolling windows of 1.6 s (black line is a Gaussian fit), and (*G*) time duration of processive motion states (black line is a log-normal fit).

NIH-PA Author Manuscript

NIH-PA Author Manuscript

NIH-PA Author Manuscript

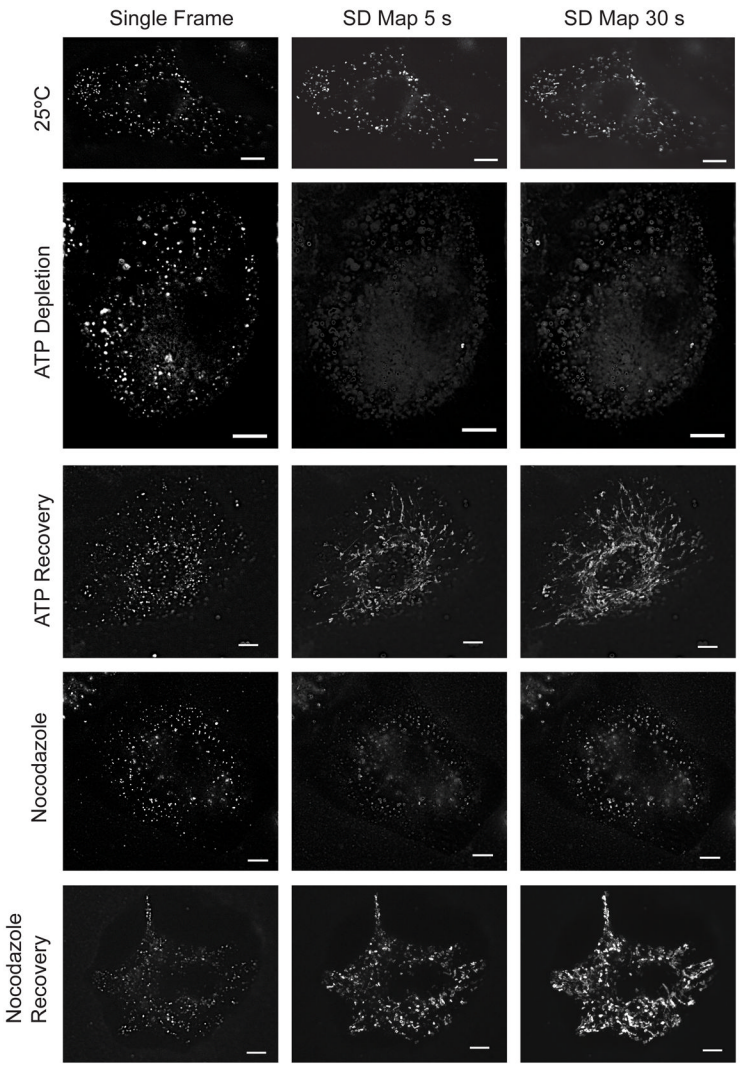

FIGURE 5.

β-actin mRNA transport depends on processive, active motion and on microtubules. (Top to bottom rows) Effects of temperature reduction, ATP depletion, recovery from ATP depletion, microtubule disruption via nocodazole, and recovery from nocodazole on mRNA transport. The left column of images shows single frames to demonstrate mRNA distribution. The middle column shows SD maps over 5 s imaging to demonstrate movements over short time scales indicative of processive motion. The right column shows SD maps over 30 S of imaging to demonstrate movements over longer time scales. Scale bars are 10 μm.

NIH-PA Author Manuscript

NIH-PA Author Manuscript

NIH-PA Author Manuscript

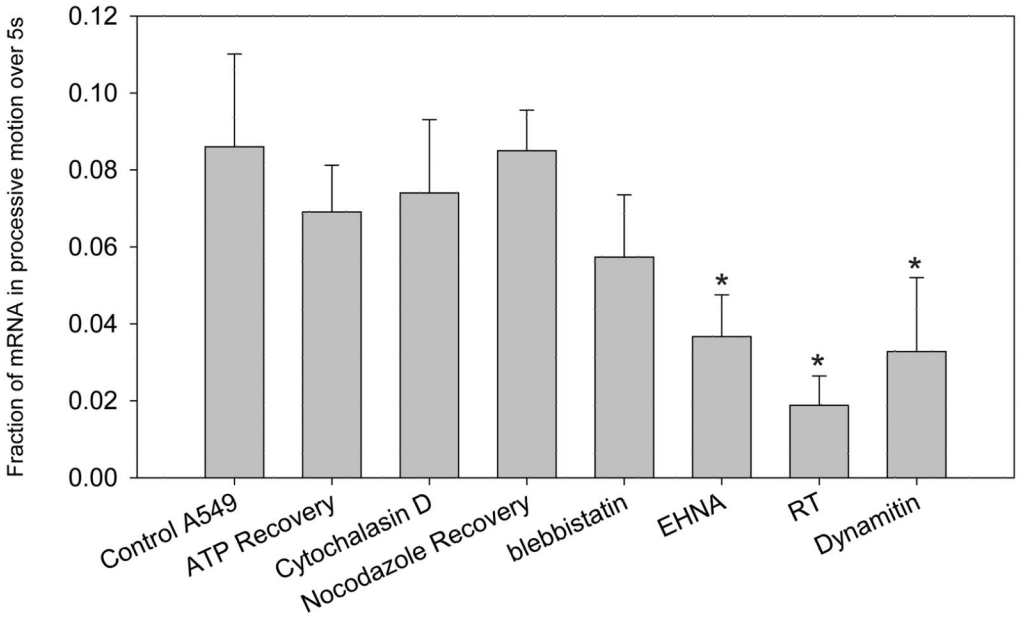

FIGURE 6.

Quantification of processive motion when A549 cells were treated with ATP depleting drugs, microtubule disrupting drugs (nocodazole), Myosin IIB inhibitor (blebbistatin), Dynein inhibitor (EHNA), when cells were incubated at room temperature (RT), when cells were recovered from ATP depletion and nocodazole treatment, and when cells were transfected with p50/Dynamitin. The fraction of mRNAs undergoing fast motion indicative of motor driven transport were calculated manually from SD maps generated over 5 s time scales. Error bars are standard deviation. Asterisks denote a statistically significant difference compared with Control A549, $p<0.05$ Kruskal–Wallis analysis of variance.

NIH-PA Author Manuscript

NIH-PA Author Manuscript

NIH-PA Author Manuscript

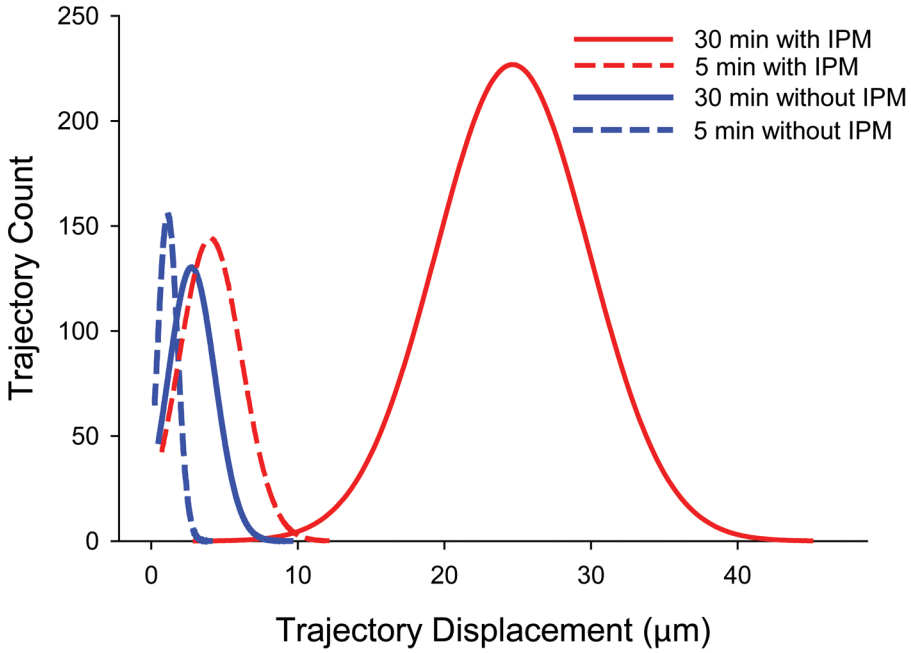

FIGURE 7.

Results of a Monte Carlo simulation using models of diffusion with and without intermittent processive motion (IPM). Trajectories were simulated for 5 min and 30 min intervals. A diffusion coefficient of 0.005 $\mu m^2/s$ and a velocity of 1 μm/s were used in the model. Plots shown are Gaussian fits of the histograms of displacements from 1000 trajectories.